The k^{-3} and $k^{-5/3}$ Energy Spectrum of Atmospheric Turbulence: Quasigeostrophic Two-Level Model Simulation

KA KIT TUNG

Department of Applied Mathematics, University of Washington, Seattle, Washington

WENDELL WELCH ORLANDO*

Colorado Research Associates Division, Northwest Research Associates, Inc., Boulder, Colorado

(Manuscript received 22 March 2001, in final form 26 September 2002)

ABSTRACT

The Nastrom–Gage energy spectrum of atmospheric turbulence as a function of wavelength is simulated here with a two-level quasigeostrophic (QG) model. This simple model has no topography, no direct wave forcing, and no small-scale forcing, nor any kind of gravity wave generation. The two-level model does, however, allow for the simple mechanism of baroclinic energy injection at the large (synoptic) scales as the model atmosphere relaxes to a specified north–south ''radiative equilibrium'' temperature gradient. It also has a small sink of energy at the small scales due to subgrid hyperdiffusion; this attempts to model the small-scale sink not resolved by the two-level QG model, in particular, enhanced viscous dissipation in atmospheric fronts. The magnitude and shape of the observed energy spectrum, with its characteristic k^{-3} power-law behavior in the synoptic and subsynoptic scales (from several thousand to about eight hundred kilometers) and the characteristic $k^{-5/3}$ behavior in the mesoscales (less than about six hundred kilometers), are reproduced convincingly in the model.

The picture that emerges for the energy spectrum of atmospheric turbulence from a few kilometers to tens of thousands of kilometers is actually quite simple. The potential energy of the mean flow, which is derived from solar heating with no scale dependence, is transferred selectively to the long synoptic scales of motion via the mechanism of (nonlinear) baroclinic instability. The injected energy moves both upscale, to the planetary waves where it is damped by Ekman damping, and also downscale, through the short synoptic waves, through the mesoscales, to the short mesoscales, where it can be damped by viscous dissipation. There is no need for dynamics other than QG to produce the spectrum. (However, the present work cannot be used to rule out other explanations, such as gravity wave generation, or a separate energy source at the small scales.)

1. Introduction

Figure 1 displays the so-called Nastrom–Gage energy spectrum in the atmosphere as a function of horizontal wavenumber. Nastrom et al. (1984) and Nastrom and Gage (1985) analyzed wind and temperature measurements taken from over 6900 commercial airplane flights during the Global Atmospheric Sampling Program (GASP) from 1975 and 1979. A majority (~80%) of these flights were over 30°–50°N in the upper troposphere and predominantly in the east–west direction or near to it. Figure 1 represents an average of these flights for each wavenumber.

It was reported by those authors that there does not appear to be a systematic difference in the spectrum over land and oceans, or between winter and summer, although the energy levels tend to be higher with increasing latitude, and the temperature variance appears to be higher in winter than in summer. A few flights were in the lower stratosphere; their temperature variance appears to be larger than in the troposphere, but this as well as the seasonal behavior is expected due to the higher static stability (as measured by the square of the Brunt–Väisälä frequency N) of the stratosphere versus troposphere and of winter versus summer; they collapse to a single curve when scaled in the form of available potential energy.

Each spectrum has two different regions with distinct slopes, which will form the focus of this work. On the longer scale, more steeply sloped region, the Nastrom–Gage spectrum agrees with previous analyses using global datasets, which showed a power-law dependence with an approximate -3 slope over the synoptic scales in the upper troposphere (Wiin-Nielsen 1967; Charney 1971; Boer and Shepherd 1983; Straus and Ditlevsen 1999). There have been many attempts to justify this

* Nee Wendell Tyler Welch.

Corresponding author address: K. K. Tung, Department of Applied Mathematics, University of Washington, P.O. Box 352420, Seattle, WA 98195-2420.
E-mail: tung@amath.washington.edu

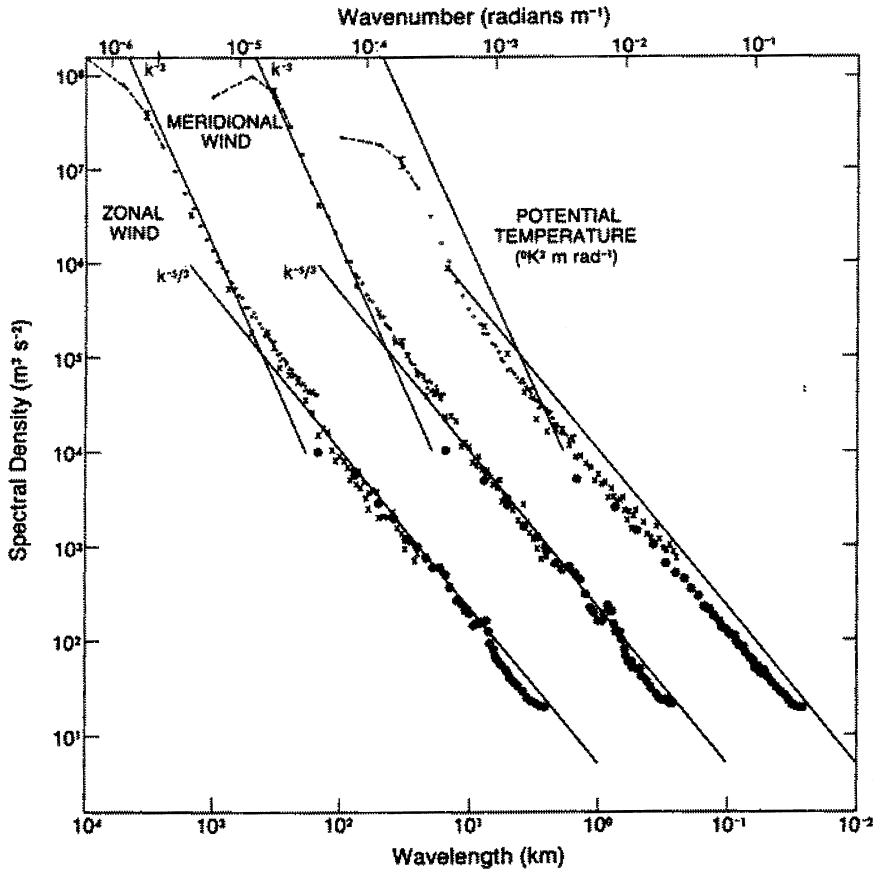

FIG. 1. Variance power spectra of wind and potential temperature near the tropopause from GASP aircraft data. The spectra for meridional wind and temperature are shifted one and two decades to the right, respectively; lines with slopes -3 and $-5/3$ are entered at the same relative coordinates for each variable for comparison. [Reproduced with permission from Nastrom and Gage (1985).]

slope theoretically. Using dimensional analysis, Kraichnan (1967) predicted a k^{-3} power law[1] for 2D, isotropic and homogeneous turbulence in a forward *enstrophy cascading inertial subrange* on the short-wave side of the scale of energy injection, as depicted schematically in Fig. 2a here. This was argued by Charney (1971) to carry over to QG turbulence and to the real atmosphere. However, part of the spectrum (from zonal wavenumber 5 to 12; i.e., wavelengths of approximately 5100–2100 km) is probably not in an inertial subrange (Lambert 1981; Boer and Shepherd 1983), as these are the scales of baroclinic instability and hence of energy injection (Welch and Tung 1998b). Furthermore, issues have been raised with Charney's arguments relating 2D and QG turbulence.[2] Even so, the shorter synoptic scales (with wavenumbers larger than 12) may indeed be close to an inertial subrange, and therefore we might expect a k^{-3} energy spectrum due to forward potential enstrophy cascade.

The Nastrom–Gage spectrum additionally shows a clear $k^{-5/3}$ power-law behavior for scales between approximately 600 and 2 km, ''the mesoscales''. This behavior had not been exhibited in previous global datasets due to a lack of resolution, but it has since been confirmed by other analyses of independent aircraft data (Marenco et al. 1998; Cho et al. 1999a,b). The smooth transition between the synoptic and the mesoscale spectrum is also noteworthy, as previously it had been thought that there would be a ''mesoscale gap'' in atmospheric turbulence energy (Fiedler and Panofsky 1970) (due to the perception at the time that the large and the small scales were driven by separate energy sources) and that this gap might have significant implication for the predictability of weather and climate (Frisch 1985).

The $k^{-5/3}$ power law has previously been predicted theoretically to occur in two distinct situations: by Kolmogorov (1941a,b) for 3D homogeneous and isotropic

[1] Kraichnan (1971) suggested a log correction to the k^{-3} leading behavior to account for the nonlocalness of the model interactions.

[2] In Tung and Welch (2001), it was pointed out that QG turbulence is not isomorphic to 2D turbulence, and so it may be problematic to apply 2D turbulence theories to the atmosphere. Furthermore, it was shown there that previous arguments and proofs against downscale energy cascade in QG turbulence using the twin conservation of energy and enstrophy were mathematically flawed.

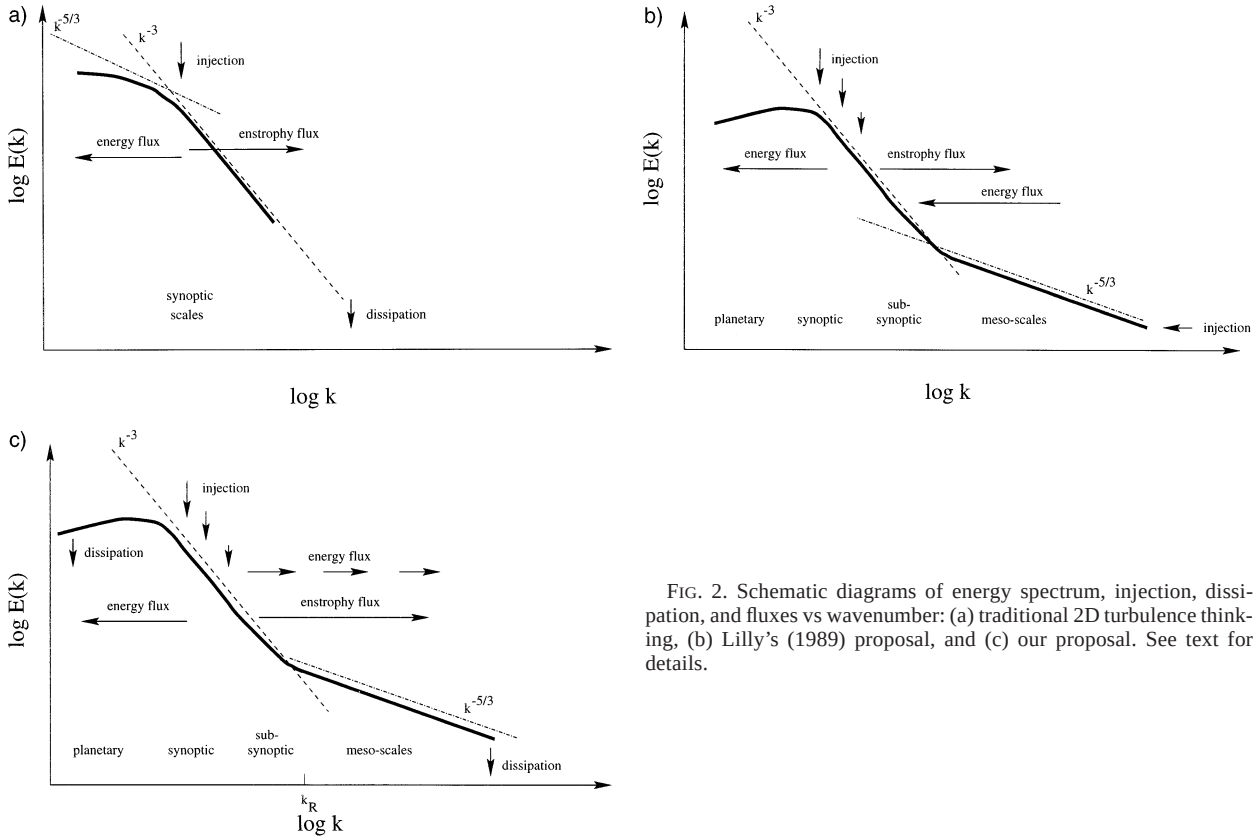

FIG. 2. Schematic diagrams of energy spectrum, injection, dissipation, and fluxes vs wavenumber: (a) traditional 2D turbulence thinking, (b) Lilly's (1989) proposal, and (c) our proposal. See text for details.

turbulence, involving a downscale energy flux, and by Kraichnan (1967) for 2D homogeneous isotropic turbulence on the *large-scale side* of energy injection, involving an *upscale* energy flux (see Fig. 2a). Frisch (1995) found it ''paradoxical'' that in the observed spectrum the $k^{-5/3}$ part occurs on the *short-wave side* of the k^{-3} part of the spectrum, in contrast to the prediction of Kraichnan (1967).

Three-dimensional turbulence arguments for the $k^{-5/3}$ spectrum rely on an assumption of isotropy in three dimensions, which is not applicable to the atmospheric mesoscales, where horizontal dimensions are much larger than the vertical dimension (except at horizontal scales of a few kilometers). It is possible that motion in the mesoscales might be isotropic in the horizontal dimensions, allowing for the possibility of 2D turbulence. Yet, because of the property of upscale energy cascade, 2D theories require a large energy source at the short-wave end of the spectrum, strong enough to pump energy upscale through several decades of scales (as in Fig. 2b). While sufficient energy can probably be provided by thunderstorms in the form of stratified turbulence or gravity waves (Lilly 1983), it is not clear that forcing at the short-wave end of the spectrum in the microscales, which are 3D, would not simply cascade energy into still shorter scales, as in 3D turbulence. Furthermore, even if a small portion of the energy (approximately 2%) could somehow escape into 2D turbulence (Smith et al. 1996) and subsequently move upscale (Vallis et al. 1997), there have been problems in simulating the spectrum with two energy sources.

First, there is the question of a sink (Larsen et al. 1982) for such an upscale energy flux in the transition region of 600–1000 km. Lilly (1989) suggested that there was probably no need for a sink for the energy cascading up from forcing at the smaller scales and for the enstrophy flux cascading down from forcing at the large scales, but numerical simulations of 2D turbulence by Maltrud and Vallis (1991) with forcing at both ends of the spectrum produced a slope steeper than k^{-3} on the long-wave side of the transition region. (Of course, this artifact may be unrelated to forcing at the small scales.) Also, the transition region itself was found to be more abrupt in the numerical result using two energy sources than in atmospheric data. Borue (1994) found, in 2D numerical simulations with a small-scale force, that with longer runs the energy spectrum in the inverse energy cascading range deviates strongly from the $-5/3$ slope and becomes closer to -3. According to the author, this was due to the emergence of coherent vortices at all scales, although the problem may simply be due to resolution. Most importantly, Gage and Nastrom (1986) pointed out that the ''remarkable degree of universality'' in spectral amplitude and spectral shape over the entire range of wavelengths encompassing both the k^{-3} and the $k^{-5/3}$ parts of the spectrum is ''hard to ex-

plain'' if it were forced by two unrelated physical processes at the two ends of the spectrum. Thus the two-source theory for the $k^{-5/3}$ portion of the spectrum is still being debated.

Recently, Koshyk et al. (1999) and Koshyk and Hamilton (2001) simulated the first spectrum showing a k^{-3} slope transitioning to roughly $k^{-5/3}$. They used a high-resolution version of the Geophysical Fluid Dynamics Laboratory SKYHI general circulation model (GCM) to produced a horizontal kinetic energy spectrum. In view of the difficulty encountered by previous attempts using 2D (and QG) models, it was natural to inquire about the role played by nongeostrophic motions, contained in the primitive equations of the GCM but not in 2D QG models. The authors pointed to the presence of a strong divergent component, which becomes comparable to the rotational part for total wavenumber $n \gtrsim 100$ in their model, and suggested an important role for gravity waves in the $k^{-5/3}$ part of the spectrum. This meshes with Yuan and Hamilton (1994), who included a divergent component in their numerical model (but with forcing only at the quasigeostrophic scales) and found a spectral regime shallower than k^{-3} in the mesoscales.[3]

The preceding results from models with nonbalanced components are indeed interesting because one of the earliest theories for the mesoscale spectrum was an extension of the internal wave theory of Garrett and Munk (1972, 1975)—which worked well for the oceanic spectrum—to the atmosphere (DeWan 1979; VanZandt 1982). However, Gage and Nastrom (1985, 1986) pointed out, with additional observational information on the vertical velocity spectrum, that there is a basic inconsistency between the observed spectra and theories of internal waves as the cause of the mesoscale spectrum. There is ''simply too much energy'' in the horizontal spectrum compared to the vertical spectrum to be consistent with the idea that both are due to a common spectrum of internal waves.

In the present work, we test the simpler hypothesis that the *entire* Nastrom–Gage spectrum can be produced by QG motion with forcing at only the large (synoptic) scales and dissipation at the small scales (i.e., viscous dissipation), as diagrammed in Fig. 2c. Between the scales of energy ''injection'' and ''dissipation'' lies a wide inertial subrange, including the k^{-3} regime and the $k^{-5/3}$ regime, spanning at least three decades of scales. Both regimes, and a transition region in between, are part of the same inertial subrange. While we acknowledge the importance of unbalanced and divergent components of the flow in contributing to the energy spectrum in the mesoscales, we test the hypothesis that they are not essential in explaining the observed $k^{-5/3}$ spectrum.

In our inertial range there is a simultaneous downscale flux of *both energy and enstrophy*. Observational support for a positive energy flux in the subsynoptic or mesoscales exists. Lambert (1981) found evidence of an inertial subrange for total spherical wavenumbers larger than 22, a downscale flux of available potential energy for almost all resolved wavenumbers, and a small downscale flux of kinetic energy over the subsynoptic scales. Straus and Ditlevsen (1999) found a small downscale flux of kinetic energy for total spherical wavenumber over 40. Recently, Cho and Lindborg (2001) pointed out a sign error in Lindborg (1999), who first argued for an inverse energy cascade in the atmospheric data over the mesoscales. When corrected, the conclusion is that their new analyses of the data ''at mesoscales in both the upper troposphere and lower stratosphere provide no support for an inverse energy cascade 2D turbulence.'' Using third-order structure functions, Cho and Lindborg calculate a downscale energy flux using observed data. We will discuss such observed values of dissipation in section 4f.

The observed features of the spectrum are simulated here numerically with a simple two-level QG model, which does not contain gravity waves. The two-level model appears to be the simplest model possessing what we believe is the relevant mechanism in the atmosphere for energy and enstrophy injection into the synoptic scales of motion: self-excited baroclinic instability drawing on the available potential energy of the mean flow, which in turn is forced by the thermal energy of the sun. As the amplifying baroclinic waves saturate nonlinearly (see Welch and Tung 1998b), a large fraction of the injected energy moves upscale, contributing to the large-scale variability of the planetary waves. A remaining small part moves downscale. In the atmosphere the downscale transfer of energy probably involves the mechanism of frontogenesis (Hoskins and Bretherton 1972), as the horizontal scales of a maturing baroclinic wave collapse near the surface and the tropopause, as well as the process of gravity wave generation by QG flows (à la Yuan and Hamilton 1994). It is likely that these small scales are then dissipated. None of these processes at the small scales can be represented by the present model, first because of the QG scaling and second because of the coarse vertical resolution. Instead we use subgrid hyperdiffusion near the scale of numerical truncation to include a crude sink at the smallest scales. As a result of this small energy sink there is a small flux of energy downscale in the model. This flux, though small, is crucial in explaining the two-sloped shape of the spectrum.

[3] It should be noted, however, that the GCM used in Koshyk et al. (1999) and Koshyk and Hamilton (2001) overpredicted the observed energy in the mesoscales, resulting in a slope shallower than the observed $-5/3$, and that some spurious gravity waves in mid mesoscales may have contributed to the overprediction. Also, Koshyk and Hamilton (2001) (like Yuan and Hamilton 1994) remarked that the divergent part of their numerical solutions were sensitive to model resolution and had not converged in the GCM results presented. In contrast, the authors demonstrated that the rotational part, including the QG motions, seemed to have converged. Yuan and Hamilton (1994) further pointed out that their spectrum was ''highly sensitive'' to both the forcing amplitude and rotation rate.

The numerical setup is presented in section 2, results in section 3, analysis in section 4, and conclusions in section 5.

2. The numerical model

The model used in our numerical experiments is a two-level QG channel model forced thermally by relaxation to a prescribed, zonally symmetric, ''radiative equilibrium'' temperature. This is the only form of forcing; there is no topography in the model. The model was documented fully in Welch (1996) and Welch and Tung (1998a,b). The model flow is damped by Ekman damping at the lower level, which, being a linear friction, affects mainly the large-scale waves, which are more energetic in the model and in the real atmosphere. This provides a large-scale sink of wave energy primarily at the planetary scales. There is subgrid dissipation at the short-wave end of the model, in a range of wavenumbers near the wavenumber of truncation, to be discussed later. This provides a sink of energy at the small scales. The model setup is thus as depicted in Fig. 2c, with sinks of energy at both the large and small scales and energy and enstrophy injection in the intermediate scales.

The dimensional form of the governing equations was given in Welch and Tung (1998a). Here we list the leveled equations, after all independent and dependent variables have been nondimensionalized:

$$\frac{\partial}{\partial t}\nabla_\delta^2\Psi_1 = -\delta J(\Psi_1, \nabla_\delta^2\Psi_1) - \delta\beta\frac{\partial\Psi_1}{\partial x} + \omega_2 - \omega_0 \quad (2.1)$$

$$\frac{\partial}{\partial t}\nabla_\delta^2\Psi_3 = -\delta J(\Psi_3, \nabla_\delta^2\Psi_3) - \delta\beta\frac{\partial\Psi_3}{\partial x} + \omega_4 - \omega_2 \quad (2.2)$$

$$\frac{\partial}{\partial t}(\Psi_3 - \Psi_1) = -\frac{1}{2}\delta J(\Psi_1 + \Psi_3, \Psi_3 - \Psi_1) - 2\sigma_o\omega_2 - 2h''[\Psi_3 - \Psi_1 - (\Psi_3 - \Psi_1)^\dagger]. \quad (2.3)$$

Here x is the longitudinal position (made dimensionless by L_x), y the latitudinal position (made dimensionless by L_y) on a β plane centered at latitude ϕ_o, p the pressure (the vertical coordinate), and t the time; Ψ is the geostrophic streamfunction, its dimensional form being defined in terms of the geopotential via $\Psi = \Phi/f_o$, and $\omega = dp/dt$ is the vertical velocity. The Jacobian $J(g_1, g_2) = (\partial g_1/\partial x)(\partial g_2/\partial y) - (\partial g_1/\partial y)(\partial g_2/\partial x)$ is made dimensionless by L_y^2; $\nabla_\delta^2 = \delta^2(\partial^2/\partial x^2) + (\partial^2/\partial y^2)$ is a Laplacian operator made dimensionless by L_y^2, that is, $L_y^2\nabla^2 = \nabla_\delta^2$ (see below for definition of δ). Subscripts 1 and 3 indicate the upper and lower levels, 2 the midpoint between levels 1 and 3, and 0 and 4 the top and bottom of the model, respectively. Also $f = f_o + \beta_o y$ is the dimensional Coriolis parameter at latitude ϕ_o, and the dagger indicates radiative equilibrium values, which are prescribed as forcing.

There are four nondimensional parameters:

$$\delta \equiv \frac{L_y}{L_x}, \quad \text{a horizontal aspect ratio}$$

$$\beta \equiv \frac{L_y\beta_o}{f_o}, \quad \text{a nondimensionalized beta}$$

$$h'' \equiv \frac{h_d'}{2f_o}, \quad \text{a coefficient of Newtonian cooling}$$

$$\sigma_o \equiv \frac{(\Delta p)^2\sigma}{2L_y^2f_o^2} = \frac{(\Delta p)^2}{2L_y^2f_o^2}\left(-\frac{1}{\rho\theta_o}\frac{\partial\theta_o}{\partial p}\right), \quad \text{a measure of static stability}$$

$$= \frac{1}{2}\left(\frac{N^2}{f_0^2}\right)\left(\frac{\Delta z}{L_y}\right)^2.$$

Here Δp is the pressure difference between model levels 1 and 3 ($\Delta z \equiv -\Delta p/\rho g$), and θ_o is a base state potential temperature, assumed not to change in time; $N^2 \equiv gd\ln\theta_o/dz$. The fluid exists on top of an Ekman layer, which yields $\omega_4 \approx -2\nu\nabla_\delta^2\Psi_3$, where ν is the Ekman damping coefficient. The upper boundary is assumed to be a rigid tropopause, such that $\omega_0 = 0$.

We restrict our attention here to the earth, for which a midlatitude ''channel'' centered at $\phi_o = 50°$ should have zonal length $2\pi L_x = 25\,700$ km and for which the width should be that of the meridional jet, that is, roughly 30° of latitude or $\pi L_y = 3340$ km. This yields an aspect ratio of $\delta = L_y/L_x = 0.26$, similar to that studied extensively in Welch and Tung (1998b). We also use a realistic β_o to give $\beta = 0.16$, and a value for Newtonian cooling time of 18 days, as in Welch and Tung (1998b). For σ_o, a measure of static stability of the atmosphere, we use an average value for winter of $\sigma_o = 0.193$.[4] The forcing is prescribed as a radiative equilibrium temperature profile across our latitude band; we have used an average winter cross-channel temperature difference of $\Delta T^\dagger = 57$ K (Lindzen 1990, Fig. 2.2; and Welch and Tung 1998a). The coefficient ν is chosen so as to yield an Ekman damping timescale of 6.7 days.

A subgrid diffusion of the form $+2\nu_s\nabla_\delta^\gamma\Psi_j$ is added to the vorticity equations (2.1) and (2.2), where the coefficient ν_s is chosen so that at the smallest scale the subgrid is equal to some multiple of the Ekman damping (see below). The order γ is chosen to concentrate the damping at the last decade of wavenumbers and to maximize the range of scales uncontaminated by the subgrid dissipation. However, γ cannot be too large or it may

[4] This is the same *dimensional* static stability for winter used in Welch and Tung (1998b), that is, $\sigma_{\text{winter}} = 2.65 \times 10^{-6}$ m^4 s^2 kg^{-2}, but the different channel widths yield different values of σ_o. Here we use a 30° wide channel such that $L_y = 1062$ km, yielding $\sigma_o = 0.193$; there a 45° channel was used such that $L_y = 1600$ km and $\sigma_o = 0.085$.

cause an effective discontinuity and hence unphysical reflections of energy from the smallest scales. We have found that $\gamma = 20$ works quite well. For all the cases shown, no reflection from the truncated wavenumbers is detected. Equations (2.1)–(2.3) are then solved by expanding in $3M \times 3N$ complex Fourier exponentials in the x and y directions, respectively. This results in $2M \times 2N$ dealiased components (using the three-halves rule to prevent aliasing), thus representing the positive and negative wavenumbers up through M and N. For example, one of the resolutions used here, 129-km resolution in the x- and y-directions, requires a computational domain of $(3M \times 3N \times 2) = (600 \times 75 \times 2)$ since there are two levels in the vertical. The highest resolution shown uses $720 \times 360 \times 2$ modes.

Two-dimensional FFTs (written by Rodney James of NCAR) are used to calculate the nonlinear terms in physical space. Simulations are started from a Hadley solution (i.e., a zonal mean state with the temperature gradient the same as the specified radiative equilibrium value). There is no initial energy in any of the waves, except for a very small random ''seeding'' of wave amplitudes for scales larger than 1000 km to allow the baroclinic instability to occur. To save time, many runs are started from the equilibrium of a previous run, which is nearby in parameter space, and are integrated forward until statistical equilibrium is established. This requires approximately 1000 time steps (116 days)[5] but 2000 time steps were allowed to ensure equilibrium. Data from running an additional 1000 or 2000 time steps (116 or 231 days), depending on the run, are then time-averaged using every tenth time step, to yield ''equilibrium'' values. Statistical equilibrium is confirmed by ensuring that energy and enstrophy dissipation rates at the smallest scales (among other measures) have become roughly constant in time.

In QG theory (Charney 1971), the total energy $\mathcal{E}$ (when integrated over the whole atmosphere) is conserved in the absence of forcing and dissipation. Note that $\mathcal{E}$ includes both kinetic and available potential energy. This is given in dimensional terms (and before leveling) by

$$\mathcal{E} = \frac{1}{2}(u^2 + v^2) + \frac{g^2}{2N^2T_o^2}T^2 = \frac{1}{2}\left[\left(\frac{\partial\Psi}{\partial y}\right)^2 + \left(\frac{\partial\Psi}{\partial x}\right)^2\right] + \frac{f_o^2}{2\sigma}\left(\frac{\partial\Psi}{\partial p}\right)^2,$$

where T_o is a reference temperature and all other symbols have their usual meanings. The total energy from observations can be obtained from the Nastrom–Gage data by summing the two horizontal velocity variances and adding the temperature variance multiplied by $(g/NT_o)^2$ (see Charney 1971), with the total sum then multiplied by 1/2. The energy displayed in this work is in the form of $E(m)$, the energy density as a function of zonal wavenumber, where

$$\mathcal{E} = \int_0^M E(m)\, dm.$$

(Note that we will use k and m interchangeably in this study to refer to zonal wavenumber.)

Similarly, the potential enstrophy, $\mathcal{Z}$, is also conserved in QG flow absent forcing and damping. It is given dimensionally, before leveling, by

$$\mathcal{Z} = \left\{ f_o + \beta y + \nabla^2\Psi + \frac{\partial}{\partial p}\left[\frac{f_o^2}{\sigma}\left(\frac{\partial\Psi}{\partial p}\right)\right]\right\}^2,$$

and the potential enstrophy density, $Z(m)$, is then defined via

$$\mathcal{Z} = \int_0^M Z(m)\, dm.$$

Although no measurement of potential enstrophy was presented from the aircraft data, potential enstrophy and its fluxes are important in QG theory. Unfortunately, analyses of global datasets (Boer and Shepherd 1983; Straus and Ditlevsen 1999) often show relative enstrophy and its fluxes instead of potential enstrophy. Relative enstrophy is not conserved in the absence of forcing and dissipation and hence is not as helpful a diagnostic. Below we will show fluxes of both total energy and potential enstrophy, though at times the adjectives ''total'' and ''potential'' will be dropped when it is understood that we are discussing QG quantities.

3. Numerical spectra

Figure 3 shows a typical energy spectrum (thick solid curve) from our numerical model at 107-km resolution. (The thick dashed curve is discussed below.) The subgrid dissipation is chosen to be 10 times Ekman damping at the last scale before truncation. This is close to the smallest value of subgrid dissipation that we can use before we encounter numerical problems.

In Fig. 3 we have, using vertical lines, separated the zonal wavelengths into the planetary scales ($\geq$8580 km; $m = 1, 2$), synoptic scales (8580 to 1980 km; $m = 3$–12;), subsynoptic scales (1980 to 640 km; $m = 13$–40) and mesoscales (2 to 640 km; $m \geq 41$). The division is made for dynamical purposes within our model (see section 4) and may not correspond exactly to common usage, although it is close. The solid and dashed curves in Fig. 3 are two separate 116-day averages, both taken after the spectrum has settled down to an equilibrium (as defined in section 2) but at different nonoverlapping times. Nevertheless, as can be seen, the large scales still have large low-frequency variability (see section 4a). This low-frequency variability is also found in real atmospheric flows (Wallace and Blackmon 1983). Apart

[5] The numerical code further subdivides this specified ''timestep'' adaptively, depending on the specified error tolerance.

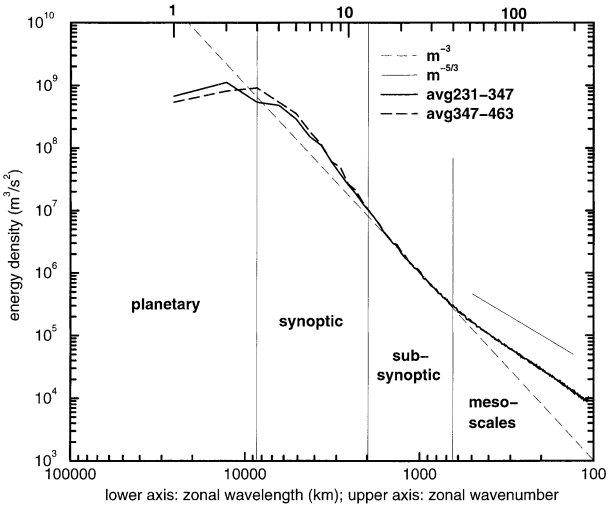

FIG. 3. Dimensional energy density vs wavelength for two 107-km runs: averaged over days 231–347 (thick solid curve) and over days 347–463 (thick dashed curve). Thin solid line has slope −5/3. Thin dashed line indicates −3 slope. Vertical lines are at $m = 3$ (8580 km), $m = 13$ (1980 km), and $m = 40$ (643 km).

from this, the spectrum has reached statistical equilibrium. As in the observed spectrum, the subsynoptic scales follow roughly a k^{-3} shape until about 800 km. Then there is a gradual transition to a $k^{-5/3}$ slope from 800 to 600 km. Note that the synoptic scales are not in the so-called inertial subrange because there is energy injection from the mean flow at these scales; the fact that their spectrum lies slightly above the −3 slope is explainable using the theory of nonlinear baroclinic adjustment (Welch and Tung 1998b).

The magnitudes of our energy spectrum compare well with Nastrom and Gage (1985). Table 1 compares the total energy density at various wavelengths from observations (Fig. 1, multiplying the temperature variance by $(g/NT_o)^2$, summing all three components and then dividing by 2; see section 2) with results from our model simulation in Fig. 3. At synoptic, subsynoptic, and mesoscales, our simulated energy density has the correct order of magnitude as the observed data, although slightly smaller. The slight—on a log scale—deficiency probably comes from the model available potential energy due to the well-known artifact of the two-level model at large horizontal wavenumbers (Merilees and Warn 1972). Thus our two-level QG model can reproduce the magnitudes, slopes, and transition wavelengths of the observations.

We show in Fig. 4 the numerical energy spectra for runs with resolution of 214, 184, and 129 km. This is less of a test of numerical convergence than of the effect of different subgrid hyperdiffusion rates. In all the cases shown, the coefficient of the subgrid hyperdiffusion is chosen such that the effective damping rate is 10 times that of Ekman friction at the last resolved scale. Thus as resolution increases, the effective small-scale dissipation rate decreases since the energy level at the last resolved scale is smaller for higher resolution. We note

TABLE 1. Approximate magnitudes of spectral energy density at various wavelengths from observations of Nastrom and Gage (1985) (Fig. 1 here) and from our QG model simulations (Fig. 3).

Zonal wavelength (km)	Energy density (m^3 s^2)	
	Observed	Simulated
2000	$1.8 – 2.0 \times 10^7$	1.0×10^7
1000	$2.5 – 2.6 \times 10^6$	1.0×10^6
100	$3.3 – 3.5 \times 10^4$	1.0×10^4

first that the k^{-3} and $k^{-5/3}$ slopes are *robust*, and are therefore probably not artifacts of numerical truncation. Even for a lower resolution of 322 km (not shown), the presence of the k^{-3} and $k^{-5/3}$ ranges is clearly demonstrated. Second, we note that as the dissipation rate is reduced—as the resolution is increased—the $k^{-5/3}$ portion moves to a lower energy level. This is consistent with the Kolmogorov scaling for the energy spectrum associated with a downscale energy flux ϵ

$$E(k) = C\epsilon^{2/3}k^{-5/3}, \tag{3.1}$$

where C is a universal constant. The downscale energy flux ϵ is equal to ϵ_D, the rate of energy dissipation at the small scales. Thus as ϵ_D is reduced, the energy level is lowered. As a consequence, the break in the slope between the −3 part of the spectrum and the −5/3 part shifts slightly to a larger wavenumber. This will be discussed more in section 4e.

The large-scale low-frequency variability seen in Fig. 3, which exists for runs with the same resolution, is also seen in Fig. 4 at the planetary scales. It should not be taken as a problem with numerical convergence.

4. Physical interpretation and diagnostics

Energy diagnostics for the 129-km resolution run are given in Fig. 5. The top panel shows the components

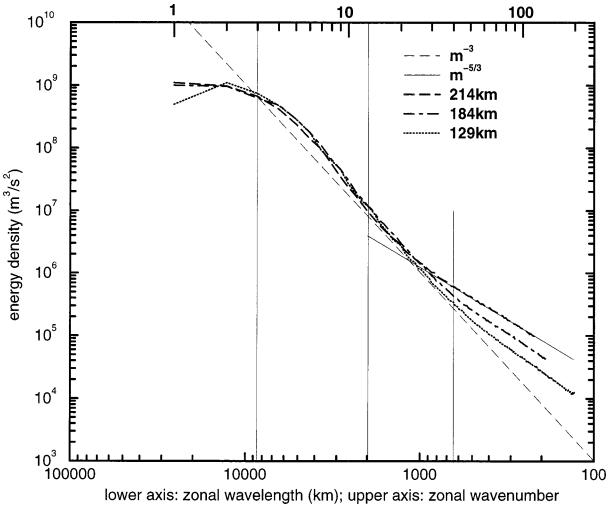

FIG. 4. Same as in Fig. 3 except for various resolutions: 214 km (long dashed), 184 km (dot–dashed), and 129 km (dotted).

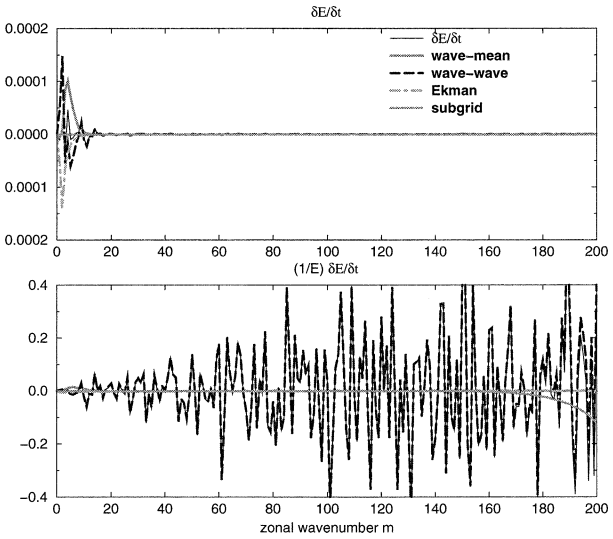

FIG. 5. Components of nondimensional perturbation energy growth rate at equilibrium for the 129-km run in Fig. 4: wave–mean flow extraction (thick solid curve); wave–wave interaction (dashed); Ekman damping (dot–dashed); subgrid dissipation (dotted); sum of all terms, a proxy for $\partial E/\partial t$ (thin solid). (top) $\partial E/\partial t$; (bottom) $(1/E)\,\partial E/\partial t$.

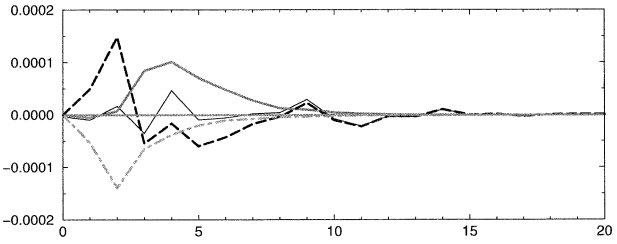

FIG. 6. Expanded versions of top panel of Fig. 5 showing only wavenumbers $m = 1$–20.

of energy change in each zonal wavenumber m, time-averaged at equilibrium: quasilinear extraction of energy from the mean flow (thick solid line); nonlinear wave–wave interaction (dashed); Ekman damping (dot–dashed); subgrid dissipation (dotted); and the sum of all these terms, which is an approximation for $\partial E(m)/\partial t$ (thin solid line).[6] For readability, an expanded version of this plot is given in Fig. 6, showing only the first 20 wavenumbers. The bottom panel of Fig. 5 is the same as the top except that each quantity has been divided by $E(m)$ for that wavenumber so as to show better the energetics of the small scales.

To diagnose the spectra of Figs. 3 and 4 we also consider the fluxes of total energy and potential enstrophy. The flux of total energy, $\epsilon(m)$, is defined from the wave–wave interaction terms in the horizontally averaged perturbation energy equation. This latter equation can be written symbolically as

$$\frac{dE(m)}{dt} = \text{wave–wave interactions}(m) + \text{wave–mean interactions}(m) + \text{dissipation}(m), \tag{4.1}$$

and the wave–wave (nonlinear) term can be written for each wavenumber as the convergence of a flux:

$$\mathcal{T}(m) \equiv \text{wave–wave interactions}(m) \equiv -\frac{\partial \epsilon}{\partial m}.$$

This expression is integrated in our discrete spectral space, imposing as boundary condition that $\epsilon(0) = 0$, to yield

$$\epsilon(m) = -\sum_{m'=0}^{m'=m-1} \mathcal{T}(m'), \qquad m = 1, M + 1.$$

Similarly, from the nonlinear terms $\mathcal{Y}(m)$ in the potential enstrophy equation analogous to (4.1), we define the enstrophy flux $\eta(m)$ by

$$\eta(m) = -\sum_{m'=0}^{m'=m-1} \mathcal{Y}(m'), \qquad m = 1, M + 1.$$

Therefore, a positive (negative) ϵ indicates a downscale (upscale) energy flux, and likewise for η. Note that the sum over all wavenumbers of the nonlinear terms in the energy equation (4.1) must be zero, since nonlinear interaction only moves energy among different scales but does not create it, and thus we must have $\epsilon(M + 1) = 0$ and similarly $\eta(M + 1) = 0$. Figure 7 shows fluxes at equilibrium for the 129-km case (discussed below) and confirms this fact.

We will now discuss the spectra of Figs. 3 and 4 using these diagnostic tools.

a. The synoptic scales: The energy injection wavenumbers

The large *synoptic scales*, with zonal wavenumbers $m \approx 3$ to 12, are the scales where "energy injection" occurs. Energy is transferred from the zonal-mean available potential energy to these waves via the mechanism of baroclinic instability (Welch and Tung 1998b). The energy injected to each wave is balanced, at equilibrium, chiefly by nonlinear energy transfers, mostly upscale to the plan-

[6] The method of Whitaker and Barcilon (1995) has been used to perform these diagnostics. Each "wave" m is a deviation from the zonal and time mean; hence, $m = 0$ here is only the time-varying portion of the zonal mean flow.

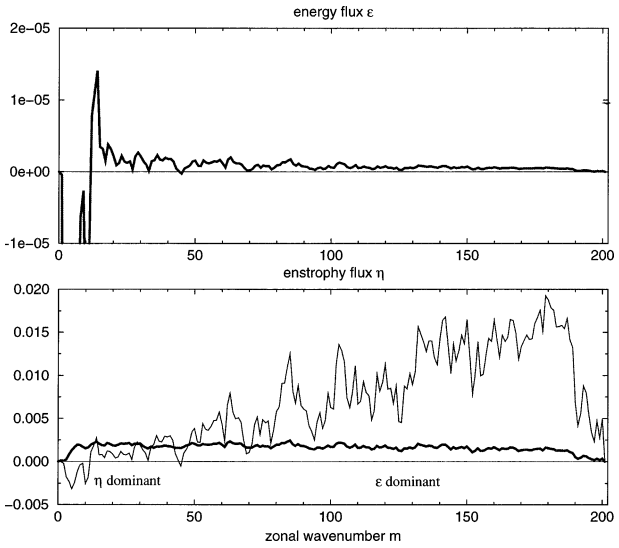

FIG. 7. Nondimensional fluxes of total energy (top) and potential enstrophy (bottom), time-averaged at equilibrium, for the 129-km case. Thin solid curve in the bottom panel is energy flux times m^2. Very thin horizontal line indicates zero flux.

etary waves but with a small amount downscale towards the subsynoptic scales and beyond, as shown in Fig. 6. The fact that this part of the energy spectrum—even in the energy injection region—approximately follows the -3 power law predicted for inertial subranges (without forcing or dissipation) is fortuitous.[7] There is, however, an explanation for this power law due to baroclinic instability, as discussed in Welch and Tung (1998b).[8]

In some previous studies this synoptic region was mistakenly identified as an inertial subrange, but such a range is only possible well away from the scales of energy injection.

b. The planetary scales

The *planetary scales*, $m = 1$–2, receive transient energy from the large synoptic scales through upscale energy transfer via wave–wave interaction. The planetary waves themselves are stable with respect to baroclinic instability (Welch and Tung 1998b) and so do not receive significant energy injection from the mean flow; the energy they gain from wave–wave transfer is balanced at equilibrium mainly by Ekman damping (Fig. 6). Some variability is evident at these scales (and for the synoptic scales as well) in Fig. 3. This is also found in analyses over time: even when statistical equilibrium has been reached in diagnostic values such as subgrid energy dissipation and subgrid enstrophy dissipation, large variability can still be seen in the energy at large scales. This can be decreased somewhat by shortening the timescale of Ekman damping (i.e., raising ν), which also decreases the level of energy in the largest scales. However, such a practice makes our model less, not more, realistic; in fact there is low-frequency variability on large scales in the real atmosphere (Wallace and Blackmon 1983). Hence we have retained our realistic timescale for Ekman damping and not attempted to eliminate all variability in, nor pinpoint the energy level of, the planetary scales.

c. The subsynoptic scales

Figures 5 and 6 show that the wave–mean flow interaction term (the energy injection) becomes insignificant for zonal wavenumbers $m \gtrsim 13$. These scales are baroclinically stable at equilibrium (Welch and Tung 1998b) and so do not receive energy from the mean flow. Their dynamics (and those of the mesoscales) are dominated by wave–wave interaction, as shown in Fig. 5 bottom.[9] As can be seen in Fig. 3, these *subsynoptic scales*, with zonal wavenumber $m \geq 13$, follow a k^{-3} power law consistent with inertial subrange theory of Kraichnan (1967) for a forward (potential) enstrophy-cascading range. To be a strict inertial range these scales would have to experience zero damping. We see from Figs. 5 and 6 that this is effectively true. As confirmation, we removed Ekman damping from all but $m = 1$–4 and found only negligible change in the spectrum or diagnostics (not shown).

These subsynoptic waves form part of an inertial subrange with the mesoscales, as discussed further in section 4d. While we leave theoretical consideration of the spectral shape to a later work, here we briefly discuss the shape in terms of simple dimensional analysis. Figure 7 shows the nondimensional fluxes of total energy and potential enstrophy at equilibrium (thick solid curves). There are *simultaneously* a *downscale potential enstro-*

[7] The slope in the energy injection region does not follow a universal power law and is dependent on the static stability N^2. This may explain why in the observed data, the slope is different at different heights in the troposphere over the synoptic scales (Boer and Shepherd 1983; Straus and Ditlevsen 1999).

[8] The wavenumbers 3–12 are linearly unstable to baroclinic instability, but their growth saturates because the earth's radiative forcing is so highly supercritical. The saturation first occurs for the linearly most unstable waves, then for the next unstable wave upscale, then the next, etc., until saturation reaches the dominant mode. The saturated part of the spectrum has a characteristic shape: the heat flux spectrum shows roughly a k^{-4} dependence, and consequently the energy spectrum is slightly steeper than k^{-3}. There is, however, height dependence in the spectral shape (see previous footnote). The spectrum is otherwise robust; it is independent of the level of forcing, as long as it is highly supercritical. This is consistent with observations, which show very little seasonal dependence of the spectrum for wavenumbers $m > 6$ [see the comparison with Randel and Held (1991) in Welch and Tung (1998b) Fig. 11], while the wavenumber of the peak heat flux shifts from 6 to 5 between summer and winter.

[9] Figure 5 bottom shows that some waves gain energy while others lose it in this time average at equilibrium. Another average taken over later times would look similar, except that some m which gained (lost) energy in Fig. 5 would now lose (gain) energy. Much longer time averages would cancel out some of these oscillations but are computationally too expensive. Note that the spectra are not altered by such variation in nonlinear interactions; Fig. 3 gives an example.

phy flux and a *downscale total energy flux,* in the subsynoptic and the mesoscales. We can determine whether the energy flux is negligible (as in an enstrophy-cascading inertial range of 2D or QG turbulence) by comparing the dimensionally equivalent ϵk^2 and η, as in the bottom panel of the figure. While both fluxes must be taken into account to describe this inertial range, in the subsynoptic scales the enstrophy flux appears to be the larger. According to Kraichnan's (1967) dimensional analysis, if the energy density $E(k)$ is a function primarily of η and k, then it must have the form $\sim\eta^{2/3}k^{-3}$, and thus the spectrum should obtain a k^{-3} spectral shape in this region.

The k^{-3} behavior in the inertial subrange blends smoothly with the energy injected wavenumbers in the large synoptic scales discussed in section 4a, although the energetics are completely different in the two regions, as seen in Figs. 5 and 6.

d. The mesoscales

The *mesoscales* in our discussion refer to scales shorter than about 600 km. (The last 10 or so wavenumbers actually form the dissipation range, which is discussed in section 4f.) We showed in Fig. 3 that the energy spectrum follows a $k^{-5/3}$ shape over the mesoscales. Dynamically, the mesoscales and the subsynoptic scales in our model form the same inertial subrange, with downscale potential enstrophy flux and downscale total energy flux present in both scale ranges (Fig. 7). In the mesoscale range, however, the energy flux is more important ($\epsilon k^2 \gg \eta$) and the shape of the energy spectrum in this range is determined to a great extent by the energy flux ϵ. From Kraichnan's dimensional analysis, then, $E(k)$ should have the form $\sim\epsilon^{2/3}k^{-5/3}$. This accounts for the $-5/3$ slope of the energy spectrum over the mesocales. Note that Kraichnan (1967) applied this thinking, instead, to the large-scale side of the energy injection wavenumbers and a negative (upscale) energy flux. In that case the flux is equal to the large-scale energy sink rate. In the present model, the downscale energy flux through the mesoscales is of order 10^{-6} m^2 s^{-3}, which is the same as the small-scale dissipation rate in the dissipation range (see section 4f). This shows that all energy fluxed to small scales is indeed being removed by subgrid dissipation.

e. The transition scale

From the discussions in sections 4c and 4d, it follows that the enstrophy flux, η, is important in the subsynoptic scales and this fact determines the $\eta^{2/3}k^{-3}$ shape of the energy spectrum there. In the mesoscales, the energy flux, ϵ, is more important and determines the shape $\epsilon^{2/3}k^{-5/3}$ in the mesoscales. At wavenumbers k such that ϵk^2 is comparable to η, the k^{-3} shape transitions to the $k^{-5/3}$ shape. It follows then that the transition wavenumber should be of the order of $(\eta/\epsilon)^{1/2}$. For example, such a calculation yields a transition wavenumber m_T of the order of $(\eta/\epsilon)^{1/2} \approx 53$ for the 129-km simulation of Fig. 7; this agrees with Fig. 4, in which the transition appears to be in the range $m = 35$–55 (450–750 km). The simulated m_T also agrees with the observed data in Fig. 1.

The relationship between η and ϵ is determined by the energy and enstrophy injection and dissipation mechanisms. The consistency between our dissipation rates and observed dissipation rates is discussed in section 4f.

f. The dissipation range

The small-scale end of the mesoscale range is actually a dissipation range, for that is where the subgrid damping becomes important. This can be seen from Fig. 5, bottom panel, to encompass the last 10 or so wavenumbers for the 129-km case (and similarly for other resolutions). Thus the last part of each spectrum in Figs. 3 and 4 is dynamically separate from the rest of the mesoscales.

The fact that the slope in the dissipation range is roughly the same as that in the mesoscale range in our simulations, that is, both about $-5/3$, is fortuitous. For other forms and magnitudes of subgrid the slope in this last group of wavenumbers would be different. In particular, for larger subgrid than used in this study, the slope in the dissipation range would be steeper than $-5/3$.

We have used a small subgrid damping magnitude, but one that is large enough to produce the downscale energy flux necessary for the two-sloped shape of the spectrum. The sink provided by our subgrid dissipation is roughly 0.5–1.1 ($\times 10^{-6}$ m^2 s^{-3}) for the simulations in Fig. 4, consistent with observed free tropospheric values (John Cho 2002, personal communication). Thus we can say that the size of the sink necessary for downscale energy flux is easily achievable in the real atmosphere.

We can also compare our enstrophy dissipation rate (i.e., enstrophy flux through the mesoscales) with observed values, at least in part. Cho and Lindborg (2001) calculated a value of 2×10^{-15} s^{-3} for *relative* enstrophy flux in the observed polar stratosphere while we obtain the same value for *potential* enstrophy flux in our simulation.

g. Observed diagnostics

For comparison, we present in Fig. 8 energetics from Straus and Ditlevsen (1999) using reanalyzed ECMWF data. The observed data agree with our model's energetics of Figs. 5 and 6, showing different balances in the different wavenumber ranges: nonlinear gain and dissipative loss in the planetary scales; baroclinic gain and nonlinear loss in the synoptic scales; and nonlinear gain and dissipative loss in the subsynoptic and mesoscales. Figure 10a of Straus and Ditlevsen (1999) also shows downscale energy flux in the mesoscales, and

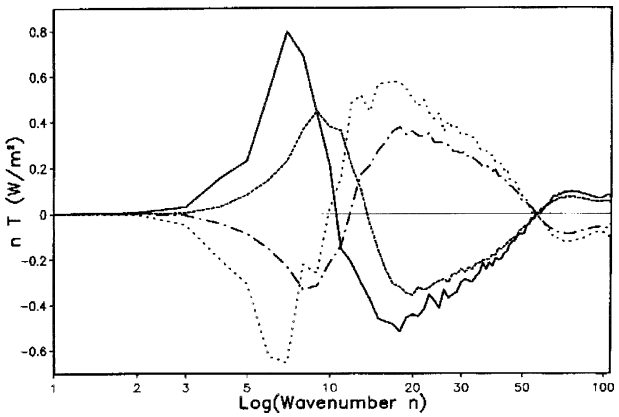

FIG. 8. Vertically integrated components of energy tendency, based on transient departures from seasonal means, multipled by total spherical wavenumber n and plotted vs log n. Solid (winter) and short-dashed (summer) curves are due to nonlinear interactions, and dotted (winter) and dot-dashed (summer) curves are due to the combination of baroclinic conversion, dissipation, vertical fluxes, and analysis increments. [Reproduced with permission from Straus and Ditlevsen (1999).]

Fig. 10b downscale enstrophy flux. Thus our model simulations with only QG dynamics are reproducing the energetics seen in observations.

5. Conclusions

Our numerical results suggest that the dynamics responsible for the observed spectrum of Nastrom and Gage appear to be rather simple and probably are already contained in a QG model. The absence of other forms of forcing other than self-excited baroclinic instability, or other (e.g., unbalanced) dynamics, does not appear to present any difficulty for the model in producing the right amount of turbulent energy in all scales of motion.

The observed energy spectrum shows a k^{-3} power law for the synoptic and subsynoptic scales of motion (5000 to 800 km) and a $k^{-5/3}$ power law for the mesoscales (600 to 2 km), with a smooth transition in between.

From dimensional arguments (similar to Kraichnan 1967) it seems that the k^{-3} part of the spectrum is associated with the enstrophy flux, η, while the $k^{-5/3}$ part of the spectrum is associated with the energy flux, ϵ. Both parts of the spectrum are present in the same inertial subrange: the k^{-3} part is dominant at the larger scales where the effect of η is felt, and the $k^{-5/3}$ part at the smaller scales where the effect of ϵ is dominant.

Our subgrid dissipation, albeit small, appears to be sufficient to ensure a downscale energy flux throughout the subsynoptic and mesoscales. In the real atmosphere such dissipation likely occurs via such processes as frontogenesis and gravity wave radiation. A two-level model cannot resolve these real physical effects but our hyperdiffusion seems to incorporate their dissipative effect, yielding a small-scale sink of energy. This in turn leads to a positive energy flux, which then produces a $-5/3$ slope in the subsynoptic and mesoscales, as in the observations of Nastrom and Gage (Fig. 1). It should be pointed out, however, that we have not done a detailed study of how our results would vary with a different form of subgrid dissipation, such as dissipating enstrophy differently from energy or with a different magnitude of subgrid dissipation coefficient.

The transition between the two slopes occurs approximately at a wavenumber k where ϵk^2 is comparable to η. The value for the transition wavenumber m_T in our simulations agrees with that of observations. The energy flux and the enstrophy flux are related by their common origin in the baroclinic energy and enstrophy injection mechanism in the synoptic scales, and their simultaneous presence in the entire range of scales on the short-wave side of the injection region, from a few thousand to a few kilometers, may be what is responsible for the robustness of the observed spectrum over wide geographical regions.

It should be pointed out that at present there is no agreement on the mechanisms responsible for the $k^{-5/3}$ power law observed for the mesoscales of motion. Almost all previous theories for the mesoscale spectrum involve treating this spectrum as separate from the -3 spectrum, either by spontaneous generation of inertial gravity waves in the mesoscale (Koshyk et al. 1999; Koshyk and Hamilton 2001) or with separate forcing of 2D turbulence at small scales (Lilly 1983; Vallis et al. 1997). The former mechanism, involving divergent and unbalanced motions, is difficult to simulate numerically, as discussed in section 1. Regarding the latter, Vallis et al. (1997) remarked that although in regions of active convection a spectrum slope close to $-5/3$ was produced by their model, given the fact that commercial aircraft measurements of Nastrom and Gage (1985) are likely biased away from regions of active convection, it is ''perhaps surprising that the measured spectra fit the $-5/3$ shape so well.''

Ours is the first proposal that involves a forward energy cascade from the synoptic-scale energy source. This is supported by observational evidence of a small but positive energy flux over the mesoscales and by a positive observed dissipation rate at the small scales. In fact, the magnitude of the dissipation used here is consistent with the observed value. Although gravity waves may play some role in contributing to the observed energy spectrum in the short mesoscales, the robustness and near universality of the Nastrom–Gage spectrum over the entire range of scales 10^0–10^4 km, and over various locations around the globe, argue for a single source of energy and enstrophy at the large scales. In our theory (see Fig. 2c) this single source is provided by the available potential energy of the mean flow supplied by the thermal energy of the sun and no small-scale source is needed.

Acknowledgments. This research is supported in part by the National Science Foundation (NSF), Climate Dynamics, under Grant ATM 9813770. Part of this work was done while WWO was a visitor at the National Center for Atmospheric Research (NCAR). Computation for the high-resolution runs were performed at NCAR. NCAR is sponsored by NSF.

We are greatly indebted to Rodney James of NCAR, who devoted many hours to help us port and parallelize our code so that higher resolution runs could be made. We also thank Dr. John Koshyk, Profs. Theordore Shepherd and Geoffrey Vallis for helpful comments, Professor Gregory Nastrom for providing us with Fig. 1 and Dr. David Straus for Fig. 8.

REFERENCES

Boer, G. J., and T. G. Shepherd, 1983: Large-scale two-dimensional turbulence in the atmosphere. *J. Atmos. Sci.,* **40,** 164–184.

Borue, V., 1994: Inverse energy cascade in stationary two-dimensional homogeneous turbulence. *Phys. Rev. Lett.,* **72,** 1475–1478.

Charney, J. G., 1971: Geostrophic turbulence. *J. Atmos. Sci.,* **28,** 1087–1095.

Cho, J. Y., and E. Lindborg, 2001: Horizontal velocity structure functions in the upper troposphere and lower stratosphere. Part I. Observations. *J. Geophys. Res.,* **106,** 10 223–10 232.

——, R. E. Newell, and J. D. Barrick, 1999a: Horizontal wavenumber spectra of winds, temperature, and trace gases during the Pacific Exploratory Missions. Part II: Gravity waves, quasi-two-dimensional turbulence, and vertical modes. *J. Geophys. Res.,* **104,** 16 297–16 308.

——, and Coauthors, 1999b: Horizontal wavenumber spectra of winds, temperature, and trace gases during the Pacific Exploratory Missions. Part I: Climatology. *J. Geophys. Res.,* **104** (D5), 5697–5716.

DeWan, E. M., 1979: Stratospheric wave spectra resembling turbulence. *Science,* **204,** 832–835.

Fiedler, F., and H. A. Panofsky, 1970: Atmospheric scales and spectral gaps. *Bull. Amer. Meteor. Soc.,* **51,** 1114–1119.

Frisch, U., 1985: Fully developed turbulence and intermittency. *Turbulence and Predictability in Geophysical Fluid Dynamics and Climate Dynamics: Proceedings of the International School of Physics ''Enrico Fermi,''* M. Ghil, R. Benzi, and G. Parisi, Eds., North-Holland, 80–84.

——, 1995: *Turbulence.* Cambridge University Press.

Gage, K. S., and G. D. Nastrom, 1985: On the spectrum of atmospheric velocity fluctuations seen by MST/ST radar and their interpretation. *Radio Sci.,* **20,** 1339–1347.

——, and ——, 1986: Theoretical interpretation of atmospheric wavenumber spectra of wind and temperature observed by commercial aircraft during GASP. *J. Atmos. Sci.,* **43,** 729–740.

Garrett, C., and W. Munk, 1972: Space–time scales of internal waves. *Geophys. Fluid Dyn.,* **3,** 225–264.

——, and ——, 1975: Space–time scales of internal waves: A progress report. *J. Geophys. Res.,* **80,** 291–297.

Hoskins, B. J., and F. P. Bretherton, 1972: Atmospheric frontogenesis models: Mathematical formulation and solution. *J. Atmos. Sci.,* **29,** 11–27.

Kolmogorov, A., 1941a: Dissipation of energy in the locally isotropic turbulence (English translation 1991). *Proc. Roy. Soc. London,* **A434,** 15–17.

——, 1941b: The local structure of turbulence in incompressible viscous fluid for very large Reynolds number (English translation 1991). *Proc. Roy. Soc. London,* **A434,** 9–13.

Koshyk, J. N., and K. Hamilton, 2001: The horizontal kinetic energy spectrum and spectral budget simulated by a high-resolution troposphere–stratosphere–mesosphere GCM. *J. Atmos. Sci.,* **58,** 329–348.

——, ——, and J. D. Mahlman, 1999: Simulation of $k^{-5/3}$ mesoscale spectral regime in the GFDL SKYHI general circulation model. *Geophys. Res. Lett.,* **26,** 843–846.

Kraichnan, R. H., 1967: Inertial ranges in two-dimensional turbulence. *Phys. Fluids,* **10,** 1417–1423.

——, 1971: Inertial range transfer in two- and three-dimensional turbulence. *J. Fluid Mech.,* **47,** 525–535.

Lambert, S., 1981: A diagnostic study of global energy and enstrophy fluxes and spectra. *Tellus,* **33,** 411–414.

Larsen, M. F., M. C. Kelley, and K. S. Gage, 1982: Turbulence spectra in the upper troposphere and lower stratosphere at periods between 2 hours and 40 days. *J. Atmos. Sci.,* **39,** 1035–1041.

Lilly, D. K., 1983: Stratified turbulence and mesoscale variability of the atmosphere. *J. Atmos. Sci.,* **40,** 749–761.

——, 1989: Two-dimensional turbulence generated by energy sources at two scales. *J. Atmos. Sci.,* **46,** 2026–2030.

Lindborg, E., 1999: Can the atmospheric kinetic energy spectrum be explained by two-dimensional turbulence? *J. Fluid Mech.,* **388,** 259–288.

Lindzen, R. S., 1990: *Dynamics of Atmospheric Physics.* Cambridge University Press, 310 pp.

Maltrud, M. E., and G. K. Vallis, 1991: Energy spectra and coherent structures in forced two-dimensional and beta-plane turbulence. *J. Fluid Mech.,* **228,** 321–342.

Marenco, A., and Coauthors, 1998: Measurement of ozone and water vapor by airbus in-service aircraft: The MOSAIC airborne program, an overview. *J. Geophys. Res.,* **103D,** 25 631–25 642.

Merilees, P. E., and T. Warn, 1972: The resolution implications of geostrophic turbulence. *J. Atmos. Sci.,* **29,** 990–991.

Nastrom, G. D., and K. S. Gage, 1985: A climatology of atmospheric wavenumber spectra of wind and temperature observed by commercial aircraft. *J. Atmos. Sci.,* **42,** 950–960.

——, ——, and W. H. Jasperson, 1984: The atmospheric kinetic energy spectrum, 10^0–10^4 km. *Nature,* **310,** 36–38.

Randel, W. J., and I. M. Held, 1991: Phase speed spectra of transient eddy fluxes and critical layer absorption. *J. Atmos. Sci.,* **48,** 688–697.

Smith, L. M., J. R. Chasnov, and F. Waleffe, 1996: Crossover from two- to three-dimensional turbulence. *Phys. Rev. Lett.,* **77,** 2467–2470.

Straus, D. M., and P. Ditlevsen, 1999: Two-dimensional turbulence properties of the ECMWF reanalyses. *Tellus,* **51A,** 749–772.

Tung, K. K., and W. T. Welch, 2001: Remarks on Charney's note on geostrophic turbulence. *J. Atmos. Sci.,* **58,** 2009–2012.

Vallis, G. K., G. J. Shutts, and M. E. Gray, 1997: Balanced mesoscale motion and stratified turbulence forced by convection. *Quart. J. Roy. Meteor. Soc.,* **123,** 1621–1652.

VanZandt, T. E., 1982: A universal spectrum of buoyancy waves in the atmosphere. *Geophys. Res. Lett.,* **9,** 575–578.

Wallace, J. M., and M. Blackmon, 1983: Observations of low-frequency atmospheric variability. *Large-Scale Processes in the Atmosphere,* B. Hoskins and R. Pearce, Eds., Academic Press, 55–94.

Welch, W. T., 1996: Nonlinear baroclinic adjustment and wavenumber selection as a mechanism for atmospheric heat transport. Ph.D. thesis, University of Washington.

——, and K. K. Tung, 1998a: Nonlinear baroclinic adjustment and wavenumber selection in a simple case. *J. Atmos. Sci.,* **55,** 1285–1302.

——, and ——, 1998b: On the equilibrium spectrum of transient waves in the atmosphere. *J. Atmos. Sci.,* **55,** 2833–2851.

Whitaker, J. S., and A. Barcilon, 1995: Low frequency variability and wavenumber selection in models with zonally symmetric forcing. *J. Atmos. Sci.,* **52,** 491–503.

Wiin-Nielsen, A., 1967: On the annual variation and spectral distribution of atmospheric energy. *Tellus,* **19,** 540–559.

Yuan, L., and K. Hamilton, 1994: Equilibrium dynamics in a forced-dissipative f-plane shallow-water system. *J. Fluid Mech.,* **280,** 369–394.